Journal of Luminescence 152 (2014) 11–14

Contents lists available at ScienceDirect

Journal of Luminescence

journal homepage: www.elsevier.com/locate/jlumin

Coherent phonon coupled with exciton in semiconducting single-walled carbon nanotubes using a few-cycle pulse laser

Takayoshi Kobayashi [a,b,c,d,*], Zhaogang Nie [a,b], Juan Du [a,b], Bing Xue [a,b]

[a] Advanced Ultrafast Laser Research Center and Department of Engineering Science, Faculty of Informatics and Engineering, University of Electro-Communications, 1-5-1 Chofugaoka, Chofu, Tokyo 182-8585, Japan
[b] JST, CREST, 5 Sanbancho, Chiyoda-ku, Tokyo 102-0075, Japan
[c] Department of Electrophysics, National Chiao-Tung University, Hsinchu 30010, Taiwan
[d] Institute of Laser Engineering, Osaka University, 2-6 Yamada-oka, Suita, Osaka 565-0871, Japan

ARTICLE INFO

Available online 31 December 2013

Keywords:
Single-walled carbon nanotubes
Coherent phonon spectroscopy
Few-cycle pulse laser

ABSTRACT

The vibrational wavepackets dynamics of single-walled carbon nanotubes (SWCNTs) are studied through the modulation of the transition probability in the visible spectral range of the systems. The modulations corresponding to the radial breathing mode (RBM), observed in the time traces for the four chiral systems (6,4), (6,5), (7,5), and (8,3), have been analyzed. The vibrational modes of the coherent phonon spectra are identified from the two-dimensional distribution of probe photon energy versus Fourier frequency. The present study pointed out that the observed probe photon energy dependence is due to both the imaginary and real parts of the third-order susceptibility, corresponding to derivative type dependence of the absorbed photon energy spectrum due to molecular-phase modulation, Raman (and Raman-like) gain and loss processes, and molecular phase modulation, respectively.

1. Introduction

Coherent phonon (CP) dynamics in single-walled carbon nanotubes (SWCNTs) have been studied by several groups, the impulsive excitation method using short pulses [1–10]. However, there are still some important concerns which need to be addressed, especially the mechanism of CP generation, which is related to coupling between the phonon modes and the excitonic state. Using a tunable laser with a 50-fs pulse duration, Lim et al. observed radial breathing mode (RBM) vibrations [2]. The oscillations in the probe transmittance were found to be the result of ultrafast modulation of the optical constants at a frequency ω_{RBM} due to band gap (E_{gap}) oscillations induced by changes in the SWCNT diameter d, which follows the relation, $E_{gap} \propto 1/d$. It was claimed that the photon energy dependence of the CP signal shows a first derivative like behavior. Although they concluded that the two spectral shapes were similar, their results showed that the CP amplitude profile was much steeper than the derivative-based profile, explained in terms of a band-gap oscillation that induces a shift in the transition absorption spectrum. The separations between the two inflection points and between the two peaks in the CP amplitude are calculated to be about 40 meV and 70 meV, respectively, using Fig. 5 of the paper [2]. The two inflection points and the two derivative peaks should be coincident if the small spectral shift is the origin of the oscillating signal. In fact, the two values differ by a factor of more than 1.7 times, and thus the real-time traces cannot simply be explained by the spectral shift mechanism.

In the present paper, we report a detailed pump–probe study of CPs in SWCNTs using sub-10-fs visible pulses and 128-channel lock-in amplifier. The latter can cover the absorption spectral range of several chiral systems with high sensitivity to the difference absorption. Thanks to the sensitivity and broad spectral coverage it has become possible to clearly compare the probe wavelength dependence and the derivatives of the absorption spectra of several carbon nanotubes (CNTs). The effects of the CPs on the difference absorbance are fully modeled. The probe photon amplitude profiles are analyzed in terms of the modulation of the excitonic transition probabilities. By doing analysis it was found that the Raman interaction and molecular phase modulation, corresponding to the imaginary and real parts of the third-order susceptibility, are found to be the origins of the probe wavelength dependence. It is reasonable since the signal from the pump–probe experiment is generated in a third-order nonlinear optical process; both the real and imaginary parts of the nonlinear susceptibility can play roles at the same time because of the Kramers–Kronig relations.

2. Experiment

The SWCNT sample was prepared by the CoMoCat method [11–13]. Details about our sub-5-fs pump–probe experimental

* Corresponding author at: University of Electro-Communications, Advanced Ultrafast Laser Research Center and Department of Engineering Science, Faculty of Informatics and Engineering, 1-5-1 Chofugaoka, Chofu, Tokyo 182-8585, Japan.
E-mail address: kobayashi@ils.uec.ac.jp (T. Kobayashi).

0022-2313/$ - see front matter © 2014 Elsevier B.V. All rights reserved.
http://dx.doi.org/10.1016/j.jlumin.2013.12.025

setup and working principle of the techniques are described elsewhere [14,15].

3. Results and discussion

3.1. Electronic relaxation and thermalization of excited population.

Fig. 1(a) graphs the two-dimensional (2D) difference absorption spectra ΔA plotted against the probe photon energy E_{pr} and the delay time t. The striped oscillatory structures parallel to the time axis represent the modulation of the difference absorbance $\delta\Delta A(E_{pr},t)$ by CPs. Here δ is the modulation of the absorbance change $\Delta A(E_{pr},t)$ due to CPs at a specific probe photon energy E_{pr} and delay time t induced by the spectral shift and transition probability change, which give rise to the horizontal and vertical modulations, respectively. Fig. 1(b) plots time-resolved spectra integrated over 200-fs delay-time steps at 10 center probe delay times ranging from 50 to 1850 fs. There are four prominent bleaching bands composed of three peaks and one shoulder, nearly coincident with the relevant E_{22} transitions for the (6,5), (6,4), (7,5), and (8,3) chiral systems. In addition, there are three isosbestic points near 2.21, 2.02, and 1.94 eV at delay times longer than 250 fs, as indicated by the small squares. The crossing points between neighboring time-resolved spectra are within ± 0.03 eV of the average photon energies, except between 0 and 50 fs. Therefore, the relaxation after 200 fs can be described using a simple two-state model composed of a single intermediate state or excited state after photo-excitation, where a conversion from one state to another is occurring. This behavior can be explained in terms of intraband relaxation from the E_{22} excitonic state to the E_{11} excitonic state, followed by a slower decay from E_{11} to the ground state.

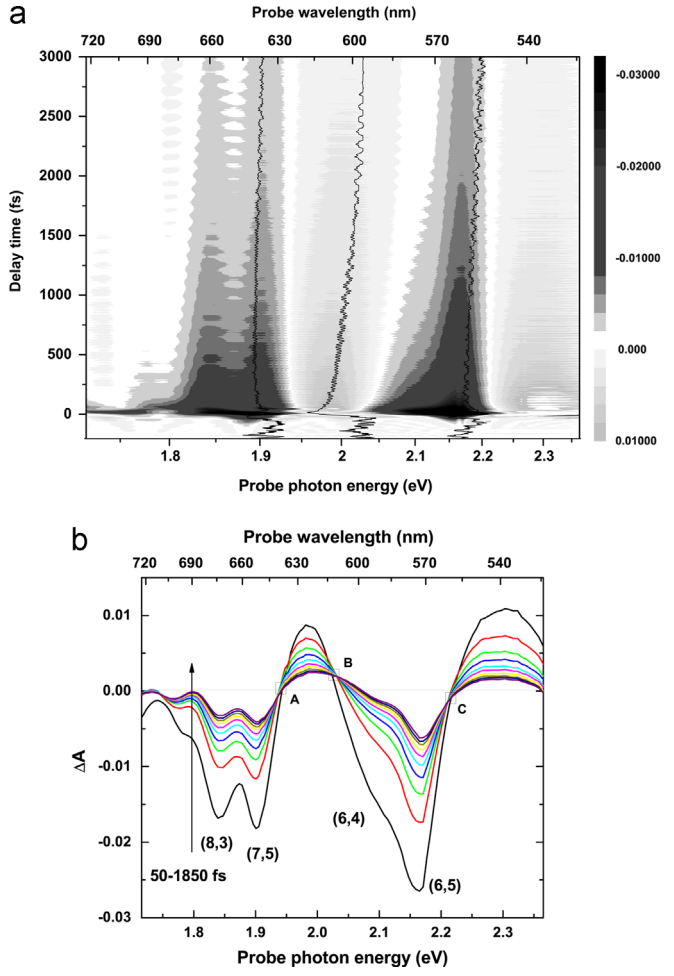

Fig. 1. (a) Two-dimensional difference absorption spectrum. The black solid curves represent the zero-change lines in the absorbance ($\Delta A=0$). (b) Time-resolved ΔA spectra at the delay time points from 50 fs to 1850 fs with a 200-fs integration step.

3.2. Fourier-transform (FT) spectra and chirality assignments

A 2D map of the Fourier power plotted against the probe photon energy and the vibrational frequency is presented in Fig. 2. The FT plots show two vibrational modes due to RBMs at $\sim$300 cm^{-1} ($\sim$100 fs) and to G modes at 1587 cm^{-1} (21 fs) [1,5,6], generated by the impulsive excitation for a pulse duration (less than 10 fs) much shorter than all the vibrational periods. Other vibrational modes are too weak to be resolved. Four RBMs are evident with vibrational frequencies of about 337, 310, 301, and 282 cm^{-1}. The assignment of chirality using only the electronic absorption or Raman spectra is often ambiguous due to spectral congestion. In contrast, the intensity of the four dominant double-peaked structures indicated by the double-headed arrows in Fig. 2 corresponds to the first derivative of the electronic absorption spectrum for the different types of tubes [2,3,6]. The central dip in each structure represents the E_{22} transition, since the oscillation is minimal at resonance [6]. However, as will be discussed later, some corrections must be made to this assertion.

The Raman shifts for different RBMs theoretically correspond to the vibrational frequencies of the FT of their CP profiles [16,17]. Consequently, the dips at the intersections of the horizontal and vertical lines in Fig. 2 correspond to the relevant vibrational frequency and electronic resonance transition energy. Using this relationship, the chirality can be assigned for the (6,4), (6,5), (7,5), and (8,3) systems, as indicated in Fig. 2, because only these tubes can simultaneously fulfill these two conditions. Other kinds of tubes may have weak absorption lines in the laser spectral range, but they cannot be efficiently excited. Using broadband high-sensitivity multichannel lock-in detectors, the power spectra of the four systems can be uniquely distinguished for RBMs, even though their absorption spectra overlap without the need for time

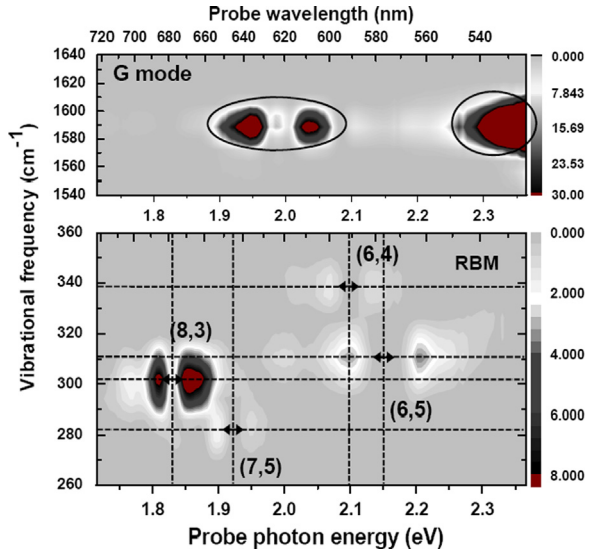

Fig. 2. 2D CP spectra in the spectral range of 1.71–2.36 eV. The chirality assignments of RBMs are shown together. In the bottom panel, the dotted crisscrossing lines show the relevant vibrational frequencies and resonance energies corresponding to RBMs. The two-way arrows indicate the double-peak structure in the amplitude profile of RBMs. The elliptic lines in the top panel display the main features observed in the G mode.

consuming or complex pulse-shaping techniques [3]. Therefore, this method is advantageous for simultaneous analysis of a sample containing many chiral systems. However, the dip position and the peak of the absorption spectrum do not exactly coincide, as will be discussed later. In contrast, for G-mode vibrations, the amplitude profiles for different chiralities overlap and cannot be distinguished. The frequency of the axial G-mode is insensitive to the diameter and chirality of SWCNTs and is thus not reflected in the location of the signal in Fig. 2.

3.3. *Fitting the amplitude spectrum with contributions from the real and imaginary parts of the third-order susceptibility*

In this section, the fit to the probe photon energy dependence of the vibrational amplitude is improved by combining the contributions from the difference (DIF)-type and derivative (DER)-type analyses. In the previous papers [2–10], based on the DER analysis, the modulation was explained in terms of a sinusoidal electronic energy modulation due to an RBM-induced change in the diameter of a CNT [2–10]. In the following, the mechanism involved in the DER-type contribution is more fully discussed.

A change in the refractive index is induced by the molecular phase modulation (MPM) process due to the DER contribution to the modulation [18]. This MPM produces a periodic shift in the probe spectrum. This in turn modulates the time-resolved spectrum composed of ground-state absorption bleaching, stimulated emission, and induced absorption. This effect results from the change in refractive index caused by the deformation of the lattice and molecular structure during the coherent vibrations [19], which the electronic distribution instantaneously follows. The index change introduces a modulation of the probe frequency because of the change in the phase of the probe field, whose time derivative is the optical frequency. Consequently, the signal can be approximated as a spectral shift of the probe pulse induced by a

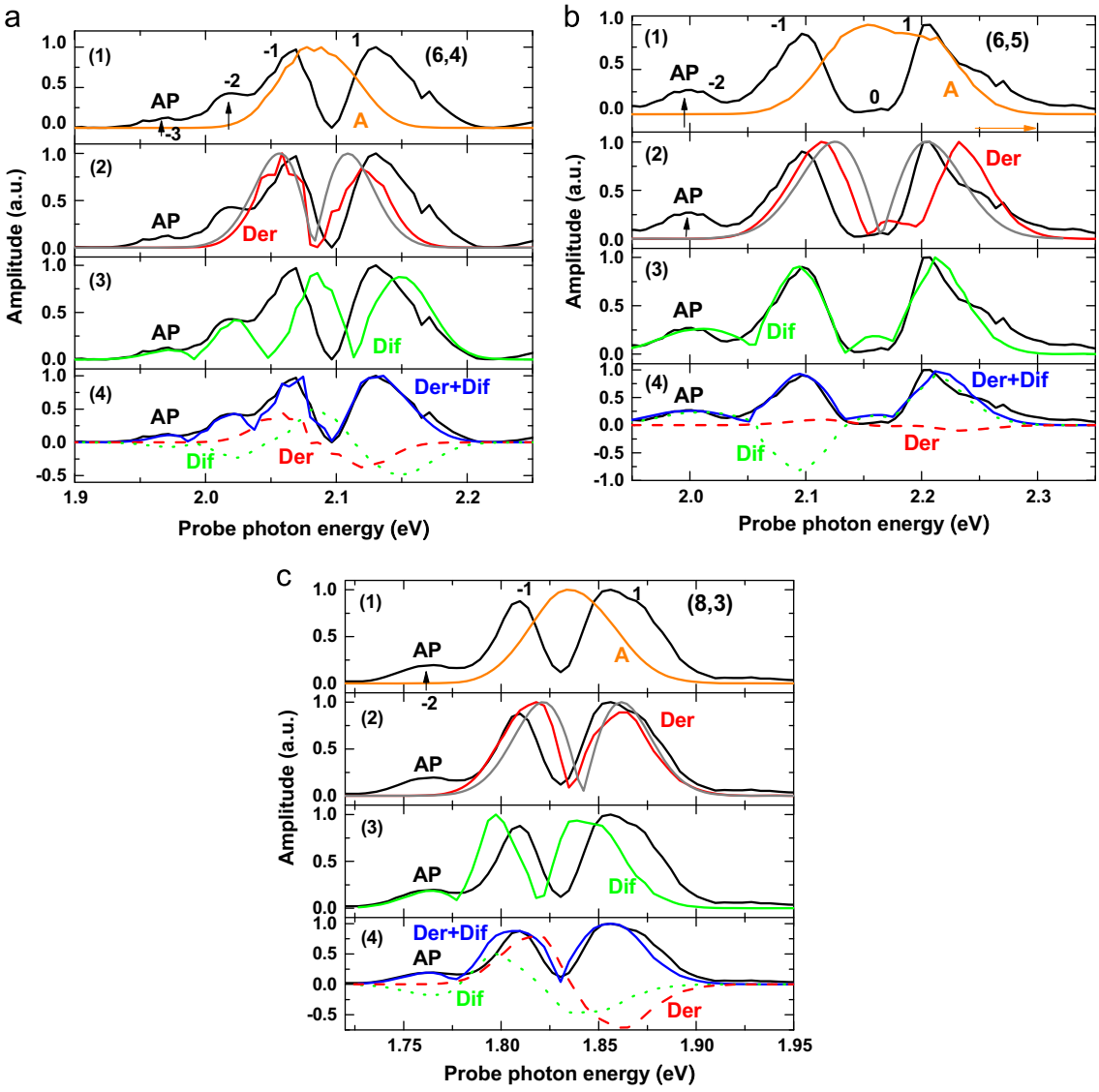

Fig. 3. Probe photon energy dependence of normalized RBM amplitude profiles (AP, black lines) for (a) (6,4), (b) (6,5) and (c) (8,3) tubes, fitted with the absorbed laser spectra (A, thin orange lines) in panels (1), first-derivative of the stationary absorptions (thin gray lines, panels (2)) and absorbed laser spectra (DER, medium width red lines in columns (2)), the absolute difference between the absorbed photon energy distribution by the sample and the distribution shifted by the relevant RBM frequency (DIF, medium thick green lines in columns (3)), and the sum of DER and DIF (DER+DIF, medium thick blue lines in columns (4)) with relevant contributions, respectively. In panels (1) and (2), the arrows indicate the side bands, and the numbers represent the peak number in amplitude profiles defined from the center band being number 0. The original DER (dashed red lines) and DIF (dotted green lines) lines in the bottom panels (4) are plotted together before taking absolute values to show their corresponding contributions to the vibrational amplitude spectra. (For interpretation of the references to color in this figure legend, the reader is referred to the web version of this article.)

kind of "cross-phase modulation" [20], and the probe energy dependence of the phonon amplitude follows the first derivative of the electronic resonance.

By adding the contributions from the DIF and DER processes, excellent fits are finally obtained, as shown in panels (4) of Fig. 3. They show the absolute value of the sum (blue lines) of the contributions of the two types of mechanisms for different RBMs with an adjustable relative contribution used as the fitting parameter for DER (dashed lines) and DIF (dotted lines) analyses, before taking absolute values of the sum. We adjusted the relative intensity of different order of phonon peaks taking into account the differences in the signs of amplitudes and adding them with the DER profile to make the fitting line shape match the amplitude profile. At first we start with the apparently reasonable ratio to fit with the experimental results of the probe photon dependence of the vibrational amplitude, and then take the sum (over probe photon energy data points) of the squared values of the difference between the fitted and observed and try to minimize the value by changing the ratio by small amount to each of the minimum deviation value. Finally we take the absolute value. The fitting profiles of DER and DIF types are already shown in panels (4) of Fig. 3 before taking absolute values.

The physical mechanisms for the DER and DIF contributions are respectively the real and imaginary parts of the third-order susceptibility. Because of the non-uniform probe spectral distribution, the (6,5) and (8,3) tubes show only anti-Stokes sidebands up to second order, while the (6,4) tubes exhibit both Stokes and anti-Stokes bands. The relative sizes of the DER contributions are further discussed below.

4. Conclusions

CP and electronic relaxation dynamics of SWCNTs were investigated in CoMoCat grown ensembles for the four chiral systems (6,4), (6,5), (7,5), and (8,3). It was found that both the imaginary and real parts of the third-order susceptibility play important roles in the modulation of the difference absorbance.

Acknowledgments

The authors would like to acknowledge Drs. H. Kataura, Y. Sakakibara, and Y. Miyata for providing us the sample.

References

[1] Gambetta, C. Manzoni, E. Menna, M. Meneghetti, G. Cerullo, G. Lanzani, S. Tretiak, A. Piryatinski, A. Saxena, R.L. Martin, A.R. Bishop, Nat. Phys. 2 (2006) 515.
[2] Y.S. Lim, K.-J. Yee, J.H. Kim, E.H. Hároz, J. Shaver, J. Kono, S.K. Doorn, R.H. Hauge, R.E. Smalley, Nano Lett. 6 (2006) 2696.
[3] J.H. Kim, K.-J. Han, N.J. Kim, K.J. Yee, Y.S. Lim, G.D. Sanders, C.J. Stanton, L. G. Booshehri, E.H. Hároz, J. Kono, Phys. Rev. Lett. 102 (2009) 037402.
[4] G.D. Sanders, C.J. Stanton, J.H. Kim, K.J. Yee, Y.S. Lim, E.H. Hároz, L.G. Booshehri, J. Kono, R. Saito, Phys. Rev. B 79 (2009) 205434.
[5] K. Kato, K. Ishioka, M. Kitajima, J. Tang, R. Saito, H. Petek, Nano Lett. 8 (2008) 3102.
[6] L. Lüer, C. Gadermaier, J. Crochet, T. Hertel, D. Brida, G. Lanzani, Phys. Rev. Lett. 102 (2009) 127401.
[7] K. Makino, A. Hirano, K. Shiraki, Y. Maeda, M. Hase, Phys. Rev. B 80 (2009) 245428.
[8] Y.S. Lim, J.G. Ahn, J.H. Kim, K.J. Yee, T. Joo, S.H. Baik, E.H. Hàroz, L.G. Booshehri, J. Kono, ACS Nano 4 (2010) 3222.
[9] J. Wang, M.W. Graham, Y.Z. Ma, G.R. Fleming, R.A. Kaindl, Phys. Rev. Lett. 104 (2010) 177401.
[10] Z. Zhu, J. Crochet, M.S. Arnold, M.C. Hersam, H. Ulbricht, D. Resasco, T. Hertel, J. Phys. Chem. C 111 (2007) 3831.
[11] M.S. Arnold, S.I. Stupp, M.C. Hersam, Nano Lett. 5 (2005) 713.
[12] S.M. Bachilo, L. Balzano, J.E. Herrera, F. Pompeo, D.E. Resasco, R.B. Weisman, J. Am. Chem. Soc. 125 (2003) 11186.
[13] Y. Miyata, K. Yanagi, Y. Maniwa, T. Tanakka, H. Kataura, J. Phys. Chem. C 112 (2008) 15997.
[14] T. Kobayashi, M. Yoshizawa, U. Stamm, M. Taiji, M. Hasegawa, J. Opt. Soc. Am. B 7 (1990) 1558.
[15] A. Baltuska, T. Fuji, T. Kobayashi, Opt. Lett. 27 (2002) 306.
[16] S.M. Bachilo, M.S. Strano, C. Kittrell, R.H. Hauge, R.E. Smalley, R.B. Weisman, Science 298 (2002) 2361.
[17] R. Bruce Weisman, Sergei M. Bachilo, Nano Lett. 3 (2003) 1235.
[18] N. Zhavoronkov, G. Korn, Phys. Rev. Lett. 88 (2002) 203901.
[19] T. Kobayashi, Z. Wang, IEEE J. Quant. Electron. 44 (2008) 1232.
[20] M.N. Islam, L.F. Mollenauer, R.H. Stolen, J.R. Simpson, H.T. Shang, Opt. Lett. 12 (1987) 625.